energy&fuels

Open Access

pubs.acs.org/EF

Article

Effect of the Temperature on Interfacial Properties of CO_2/H_2 Mixtures Contacting with Brine and Hydrophilic Silica by Molecular Dynamics Simulations

Cheng Chen, Jun Xia,* and Hamid Bahai

Cite This: *Energy Fuels* 2023, 37, 18986−18995

Read Online

ABSTRACT: Underground H_2 storage (UHS) is a promising technology to achieve large-scale, long-term H_2 storage. Using CO_2 as a cushion gas to maintain the pressure of the reservoir and withdraw stored H_2 in the saline aquifer simultaneously enables the implementation of UHS and underground CO_2 storage (UCS). The difference in the molecular properties of CO_2 and H_2 leads to distinct interfacial behavior when in contact with the brine and rock, thereby affecting the flow patterns and trapping mechanisms of gases in geological formations. Accurate prediction of the interfacial properties of CO_2, H_2, and the mixtures when interacting with brine and rock is crucial to minimizing the uncertainties in UHS and UCS projects. In this study, molecular dynamics (MD) simulations are performed to predict the interfacial tension, surface excess, bubble evolution, and contact angle of CO_2, H_2, and the mixtures at 10 MPa and 300−400 K. The MD results show that the interaction of CO_2 with H_2O and hydrophilic silica is considerably stronger than that of H_2. The interfacial tension reduces linearly with the temperature in H_2-dominated mixture systems, and the surface adsorption of H_2 can diminish in a CO_2-dominated system or at high-temperature conditions. The hydrophilic silica is more CO_2-wet than H_2-wet, and the attached CO_2 bubble is more easily disconnected. Ions and the temperature play different roles in the contact angle.

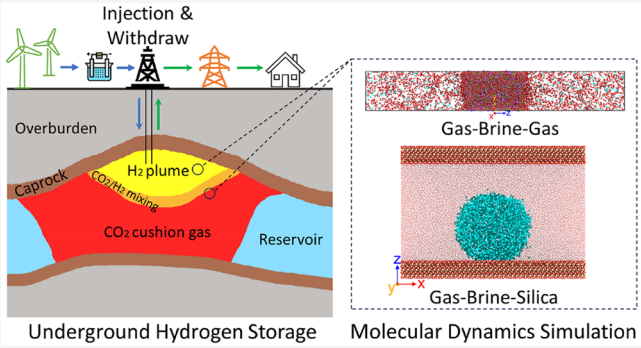

1. BACKGROUND

CO_2 capture, utilization, and storage (CCUS) plays a key role in achieving net zero. According to the International Energy Agency (IEA) assessment of the net-zero trajectories, the demand for CO_2 storage is projected to escalate significantly from approximately 40 Mt/year to more than 5000 Mt/year by 2050.[1] The underground CO_2 storage (UCS) is the vital cornerstone of the CCUS value chain, in which captured CO_2 is compressed, transported, and injected into the deep undersurface reservoir and finally trapped by the geological porous formations. According to the IEA estimation, the global UCS capacity can be 8000−55 000 Gt.[2] More recently, injecting H_2 into the reservoirs and achieving the underground H_2 storage (UHS) is proposed to meet the demand of large-scale and long-term (GWh/TWh and weeks−seasons) storage. Some pilot projects show the feasibility of UHS. For example, a mixture of 3−4% CO_2 and 95% H_2 has been stored in a salt cavern in Teesside, U.K., at the depth of 400 m.[3] During the UHS process, CO_2 can be used as cushion gas to maintain the pressure and withdraw stored H_2. This indicates that CO_2 working as a cushion gas in UHS is a new CO_2 utilization scenario, which can facilitate the deployment of UCS and UHS simultaneously.

The potential site options for underground gas storage (UGS) mainly include depleted gas/oil reservoirs, coal seams, deep saline aquifers, and salt caverns, which differ by their location, quantity, formation component, seal property, and storage capacity. Although a salt cavern is relatively impermeable and has a high level of containment integrity, it has limited quantity and smaller storage capacity.[3] Depleted gas/oil reservoirs and saline aquifers are porous media containing considerable amounts of nanopores,[4] and deep saline aquifers exhibit a potential capacity of 2000−13 000 Gt.[2] The injection of a large volume of CO_2 into deep saline aquifers will displace the resident fluids and induce the multiphase fluid flow, followed by the solute transport and chemical reactions between fluids and formation minerals. To be specific, the injected gases would flow upward as a result of the buoyant effect and the density difference until reaching the impermeable layer of tight caprock,

Received: August 21, 2023
Revised: October 5, 2023
Accepted: October 6, 2023
Published: November 8, 2023

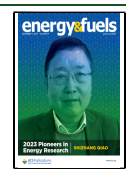

https://doi.org/10.1021/acs.energyfuels.3c03164
Energy Fuels 2023, 37, 18986−18995

which is known as the structural trapping. As CO_2 continues to migrate within the aquifer, a fraction of it can remain as isolated or residual bubbles or droplets in the pore spaces. The CO_2 plume is split into numerous micrometer-scale bubbles or droplets, which are immobilized by the capillary forces within the pore network of the rock, which is referred to as the residual trapping.[5] At the interface between CO_2 and brine, a portion of CO_2 can dissolve into the brine and generate mild carbonic acid (H_2CO_3). Bicarbonate can react with the minerals and transform into solid carbonate minerals, achieving permanent trapping. These four different trapping mechanisms (structural trapping, residual trapping, dissolution trapping, and mineral trapping) account differently for storage capacity and safety. Unlike UCS, the dissolution trapping and geochemical reactions, such as methanogenesis in UHS, can lead to the significant loss of H_2 which are absolutely unfavorable.[6]

The intermolecular interaction of the gas−liquid−rock system determines the capillary entry pressure (P_{ce}) required for gas penetration in the pores. P_{ce}, in turn, significantly affects the structural trapping capacity of the caprocks and the efficiency of residual trapping in deep saline aquifers.[5,7,8] P_{ce} can be calculated by the Young−Laplace equation

$$P_{ce} = P_g - P_l = \frac{2\gamma_{gl}\cos\theta}{R} \tag{1}$$

where P_g is the pressure of the gas phase, P_l is the pressure of the liquid phase, γ is the interfacial tension (IFT) of gas and liquid, θ is the contact angle (CA), and R is the pore through radius.

The maximum column height, h (i.e., volume), of gas immobilized beneath the caprock[7,9] is expressed as

$$h = \frac{P_{ce}}{\Delta\rho_{gl} g} = \frac{2\gamma_{gl}\cos\theta}{R\Delta\rho g} \tag{2}$$

where $\Delta\rho$ is the gas−liquid density difference and g is the gravitational constant.

Clearly, it is crucial to accurately predict the basic properties, such as the density, IFT, and CA, at reservoir conditions for reliable evaluations of the UCS and UHS projects. In general, the conditions of the saline aquifer vary with the depth following roughly that T (°C) = 15 + 33d and P (atm) = 1 + 100d, where d is the depth in kilometers.[10] The typical conditions of UCS and UHS are in the range of 300−400 K and 5−25 MPa;[5,9,11] thus, CO_2 (T_c = 304.13 K and P_c = 7.38 MPa) is in liquid or supercritical conditions, while H_2 is more likely in its supercritical conditions (T_c = 33.15 K and P_c = 1.30 MPa). Captured CO_2 from the steam methane reforming process or from a steel mill can always have impurities, such as H_2S, CH_4, and H_2. The impurities in CO_2 can affect its solubility, injectivity, and storage capacity.[12−14] It was found that the difference among H_2, CO_2, and H_2O regarding the density, viscosity, IFT, and wettability can lead to the complicated flow patterns and displacement process, such as the viscous/capillary fingering structures.[3,15,16] However, to the best of our knowledge, the interfacial properties of CO_2/H_2 mixtures in contact with brine and rock are extremely lacking.

A substantial number of experiments and modeling studies, mainly the molecular dynamics (MD) simulation, have been performed in context of UCS. More recently, a few unsystematic works were also performed for UHS. For example, vapor−liquid equilibrium (VLE) MD simulations have been performed for the CO_2−brine/oil systems[17,18] and H_2−brine system[19] with pressure up to 100 MPa, which accurately predicted the surface excess adsorption and the IFT. Although having huge uncertainties in experiments,[20] the consensus is reached that CA of water increases with the pressure of CO_2 because the increased CO_2 density can enhance the CO_2−rock intermolecular interactions.[5] MD simulation results of the CA using the CO_2−H_2O (in sessile droplet)−rock system at pressures up to 50 MPa[11,21] also follow the trend. In the experimental measurement of the water CA in the H_2−brine−clay system using the sessile droplet method, it was found that cos(θ) correlates linearly with the H_2 density when contacting with some typical clay mineral slabs, such as montmorillonite, illite, and kaolinite.[22,23] However, the MD simulation by Al-Yaseri et al.[24] found that H_2 is completely non-wetting and CA is independent of the H_2 pressure in both H_2−H_2O−quartz and H_2−H_2O−calcite systems, and they emphasized the necessity to clean the mineral samples to avoid the surface contamination-induced uncertainties. The research on UHS is still in its infancy, and reliable interfacial properties of H_2 contacting with brine and rock are highly needed.[9] The effect of the temperature on CA is still an open question, and more research is highly needed to understand the mechanism.[5,22,25]

High-pressure, wide-range temperature conditions cause many difficulties in experiments particularly considering the flammability of H_2. In this study, MD simulation is performed to investigate the effect of the temperature (300−400 K) on interfacial properties of the CO_2/H_2−brine system and the CA of the brine−CO_2/H_2−rock system using the captive bubble method at an isobaric condition of 10 MPa. The paper is organized as follows: molecular models and force fields of the components, including CO_2, H_2, H_2O, NaCl, and a silica model representing the hydrophilic rock, are given in section 2.1. The system configuration and MD setup of the gas−brine two-phase system and gas−brine−rock three-phase system are given in section 2.2. The results of interfacial properties of the two-phase system are given in section 3.1. The effect of the bubble size on morphology evolution is given in section 3.2. The effect of the temperature on CA is given in section 3.3. Finally, the conclusion is given in section 4.

2. MD SETUP

2.1. Molecular Model and Force Field. The intra- and intermolecular interactions are described by the force field. In this study, the transferable potentials for phase equilibria (TraPPE) force field developed by Potoff et al.[26] was used for CO_2 molecules, with flexible bonds and angles. The parameters of bond stretch and angle bend are taken from the work of Zhong et al.,[27] which have been validated against experimental data on transport properties over a wide range of conditions. The Madrid-2019 ion model developed by Zeron et al.[28] based on the TIP4P water model[29] was used for brine, in which the ion charge of Na^+ and Cl^- is scaled by 0.85 for better description of the infinite dilution properties. It was demonstrated that this set of force fields can be used to model the practical seawater, with excellent prediction on transport properties, structural properties, and interfacial properties.[30] The interface force field (IFF) developed by Wang et al.[31] and Heinz et al.[32] are used for H_2 molecules and Q2 silica (9.4 silanol groups/nm^2), respectively. The IFF force field has been used widely in the CO_2−H_2O−silcia system to predict the contact angle and wettability.[11,21]

The force fields are compatible with each other as they use the same formula to describe the potential energy of the MD systems, expressed as

https://doi.org/10.1021/acs.energyfuels.3c03164
Energy Fuels 2023, 37, 18986−18995

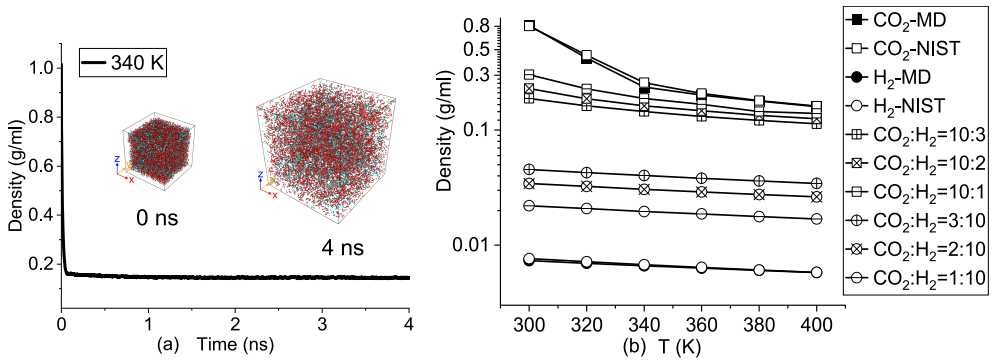

Figure 1. (a) Time evolution of the density and snapshots of the bulk MD system containing 10 000 CO_2 and 3000 H_2 molecules. (b) Effect of the temperature on the density of CO_2, H_2, and CO_2/H_2 mixtures.

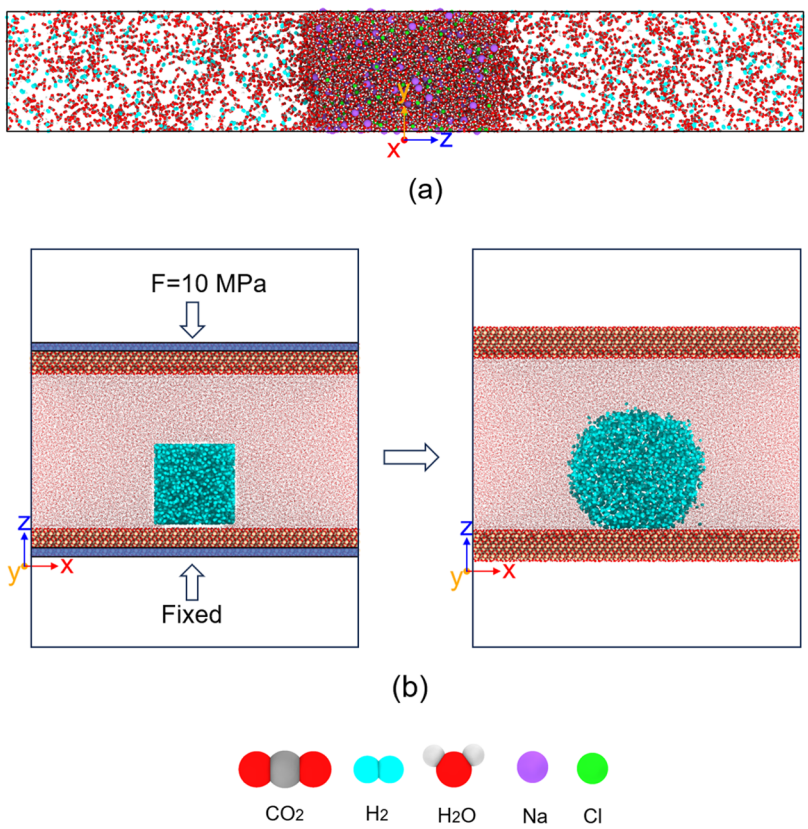

Figure 2. (a) Gas−brine system after equilibrium. The brine film contains 10 000 H_2O molecules and 400 Cl^+ and 400 Na^+ ions. The thickness of the brine film is about 8.8 nm. The box length is $(L_x, L_y, L_z) = (6, 6, 40)$ nm. (b) Equilibrium process of the system: H_2O-H_2-silcia. $(L_x, L_y) = (20.8, 10.3)$ nm for the Q2 slab. The number of H_2O molecules is 60 000. The atoms in the shaded area are added via the external force. The atom vdW radius of H_2 is scaled by a factor of 2, while the atom radius of H_2O is scaled by 0.2 for visualization.

$$E = 4\varepsilon_{ij}\left[\left(\frac{\sigma_{ij}}{r_{ij}}\right)^{12} - \left(\frac{\sigma_{ij}}{r_{ij}}\right)^{6}\right] + \frac{q_i q_j}{4\pi\varepsilon_0 r_{ij}} + k_b(b - b_0)^2 + k_\theta(\theta - \theta_0)^2 \quad (3)$$

where the first two terms are the non-bonded interactions of van der Waals (vdW) force and electrostatic force, while the last two terms are intramolecular energies of the bond stretch and angle bend, i and j are indices of atoms, ε and σ are energy and size parameters of the Lennard-Jones (LJ) potential, q is the charge of the atom, ε_0 is the vacuum permittivity, r_{ij} is the distance between two atoms i and j, k_r and k_θ are the energy constants, b and θ are the bond length and angle of two bonds, and b_0 and θ_0 are the equilibrium values. The other intramolecular energies of dihedral and out of plane are not considered for silica.[33] The interaction of different particle types is described by the Lorentz−Berthelot combining rules: $\sigma_{ij} = (\sigma_{ii} + \sigma_{jj})/2$ and $\varepsilon_{ij} = (\varepsilon_{ii}\varepsilon_{jj})^{1/2}$.

2.2. MD Setup and System Configuration. All MD simulations are performed using the package of Large-scale Atomic/Molecular Massively Parallel Simulator (LAMMPS),[34] and the visualization is performed using the Open Visualization Tool (OVITO).[35] The cutoff distance for vdW and electrostatic interactions is 1.4 nm. The particle−particle particle−mesh (PPPM) solver with an accuracy of 1×10^{-5} is used to compute the long-range electrostatic interaction.

The bulk MD system is built as shown in Figure 1 to validate the force field of CO_2 and H_2 as well as compute the density of the gas mixture. In addition to the systems of pure CO_2 and H_2 gases, two other binary gas mixture systems are also built. One is dominated by CO_2, while H_2 is added as an impurity with the mole ratio of H_2/CO_2 equal to 1:10, 2:10, and 3:10. The other one is dominated by H_2, while CO_2 is

https://doi.org/10.1021/acs.energyfuels.3c03164
Energy Fuels 2023, 37, 18986−18995

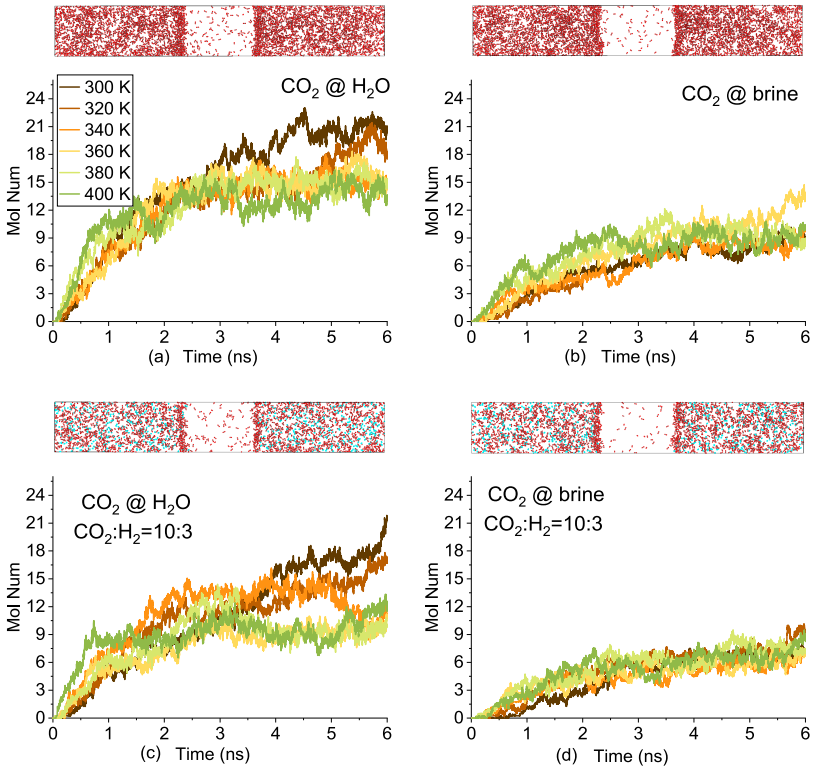

Figure 3. Time evolution of the CO_2 molecule number in the region of $-2.5 < z < 2.5$ nm in different systems: (a) CO_2 contacting with H_2O, (b) CO_2 contacting with brine, (c) CO_2 and H_2 mixtures contacting with H_2O (gas molar ratio of CO_2/H_2 = 10:3), and (d) CO_2 and H_2 mixtures contacting with brine (gas molar ratio of CO_2/H_2 = 10:3). Snapshots are at 6 ns and 340 K. Brine molecules are hidden.

added as an impurity with the mole ratio of CO_2/H_2 equal to 1:10, 2:10, and 3:10. Gases are equilibrated in the *NPT* (constant pressure/temperature, where *N* is the number of molecules, *P* is the pressure, *T* is the temperature) ensemble for 4 ns with a time step of 1 fs. Periodical boundary conditions in all three directions are implemented in the bulk MD simulation.

The system at 340 K reached equilibrium after 63 ps, as shown in Figure 1a, and the density of Figure 1b is the averaged data of the last 2 ns *NPT* simulation. The density of pure CO_2 and H_2 from MD simulation agrees well with the National Institute of Standards and Technology (NIST) data. The effect of the temperature on the CO_2 and CO_2-dominated systems is much more prominent than that of H_2 and H_2-dominated systems.

The gas−brine two-phase system and brine−gas−silica three-phase system are built to study the interfacial properties, as shown in Figure 2. The mole ratio of the ion with H_2O is 4% (2.22 M in molality), which is relatively higher than seawater considering that the evaporation-induced salt precipitation would always occur during the injection. For the two-phase system as shown in Figure 2a, the periodical boundary conditions are implemented in all directions. The box length is the same in all systems, and the number of gas molecules is calculated and packed into the box according to the gas density in Figure 1 to keep the pressure at about 10 MPa.

The number of gas molecules varies in the three-phase system, as shown in Figure 2b, to study the effect of the bubble size on morphology evolution. The pressure is controlled by adding external forces on portion atoms of the top slab, while the position of the bottom slab is fixed.[36] The periodical boundary conditions are implemented in *x* and *y* directions, while fixed non-periodical boundary conditions are used in the *z* direction with a vacuum space of 5 nm to virtually turn off the interactions between the slabs.

3. RESULTS

3.1. Effect of the Temperature on Interfacial Properties of the Gas−Brine System. The time evolution of the CO_2 molecules in the middle brine film region of $-2.5 < z < 2.5$ nm is shown in Figure 3. CO_2 molecules accumulate at the interface and diffuse into H_2O films after they reach saturation, as shown in Figure 3a. A higher temperature indicates higher diffusivity but lower solubility, as CO_2 molecules reach a plateau much faster at 400 K than 300 K, with the value almost been halved. This agrees well with the work of Shiga et al.,[37] in which the solubility of CO_2 reduced by about 50% at 10 MPa when the temperature is increased from 300 to 400 K. H_2 can also accumulate slightly or even be unidentifiable at the interface, and only a few H_2 molecules diffuse into the middle region (not shown). NaCl slows the diffusion and reduces the solubility of CO_2, as shown in Figure 3b. The effect of the temperature on CO_2 solubility in brine is not as evident at that in H_2O. Adding 30% H_2 into CO_2 does not evidently alter the diffusivity and solubility of CO_2 in both H_2O and brine.

After systems reach equilibrium, the density profile $\rho_i(z)$ of the gases and water is computed and demonstrated in Figure 4. The surface excess (Γ) and enrichment (E) are used to characterize the gas−liquid interfacial adsorption property based on the density profile. The surface excess of component *i* relative to *j* ($\Gamma_{i,j}$) is used to quantify the relative adsorption tendency of *i* to *j* in the interface, expressed as[38−40]

$$\Gamma_{i,j} = -(n_i^{\mathrm{I}} - n_i^{\mathrm{II}}) \int_{-L_z/2}^{L_z/2} \left[\frac{n_j(z) - n_j^{\mathrm{I}}}{n_j^{\mathrm{I}} - n_j^{\mathrm{II}}} - \frac{n_i(z) - n_i^{\mathrm{I}}}{n_i^{\mathrm{I}} - n_i^{\mathrm{II}}} \right] \mathrm{d}z \tag{4}$$

or specifically gas *i* to water in Figure 4 can be computed by the following equation:[39]

https://doi.org/10.1021/acs.energyfuels.3c03164
Energy Fuels 2023, 37, 18986−18995

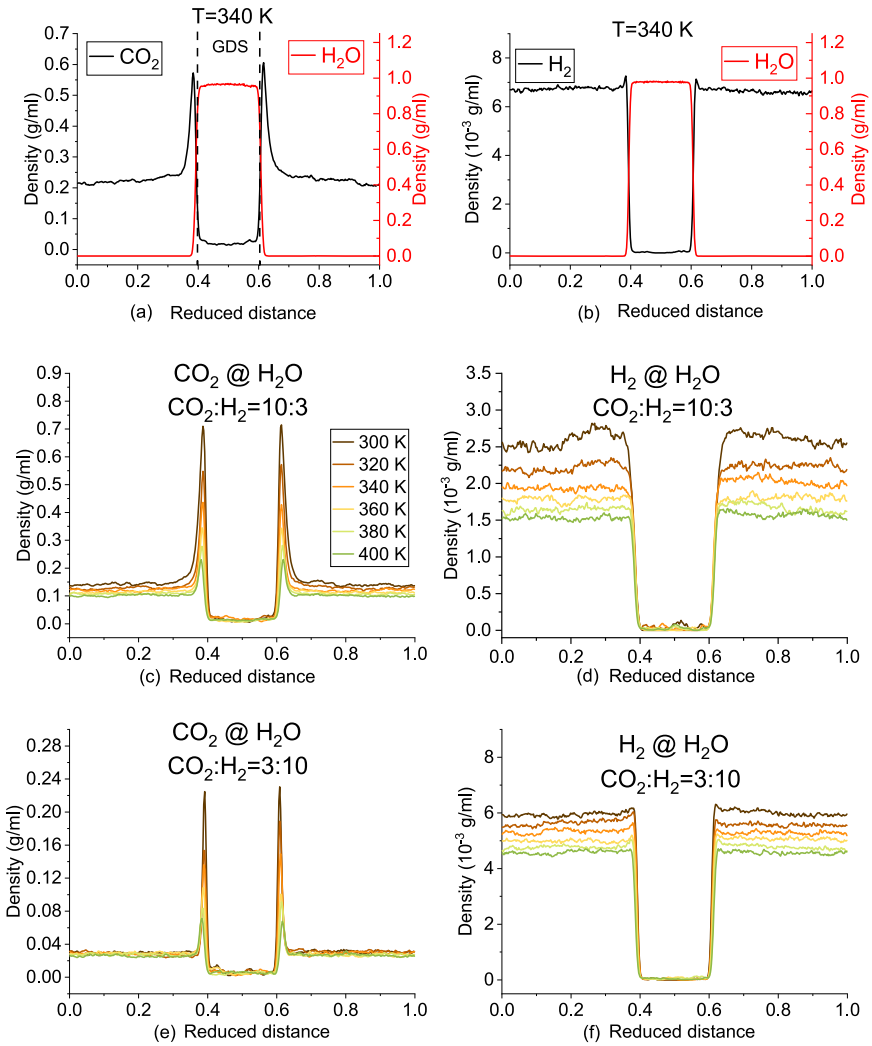

Figure 4. Density profile of CO_2, H_2, and H_2O in different systems: (a) CO_2-H_2O system at 340 K, (b) H_2-H_2O system at 340 K, and (c−f) CO_2/H_2 mixtures−H_2O system at different temperatures. The dashed lines in panels a and b are to indicate the position of the GDS.

$$\Gamma_{i,\mathrm{w}} = \frac{N_i^{\mathrm{total}} - n_i^{\mathrm{I}} V_{\mathrm{I}} - n_i^{\mathrm{II}} V_{\mathrm{II}}}{A} \tag{5}$$

where n is the number density, N is the total number of gas molecules, I and II denote the gas-rich bulk phase and water-rich bulk phase, distinguished by the Gibbs dividing surface (GDS), V is the volume of phase I or II, and A is the area of the interface. The GDS is used to identify the position of the interface where the surface excess of water is zero from the density profile of water;[38,39] i.e., $\Gamma_{\mathrm{w,w}} = 0$.

The interfacial enrichment of component i is defined as[40]

$$E_i = \frac{\max(\rho_i(z))}{\max(\rho_i^{\mathrm{I}}, \rho_i^{\mathrm{II}})} \tag{6}$$

At 340 K, the density of water increases monotonously from vapor to liquid phase, while the density of the gases exhibits a peak at the interface for both CO_2 and H_2 because of the surface activity.[41] The enrichment of CO_2 is much higher than that of H_2 at 340 K, and CO_2 has a thicker adsorption layer than H_2. In the CO_2/H_2 mixture system, the enrichment of CO_2 is enhanced, while that of H_2 is reduced. In the CO_2-dominated system, the surface adsorption of H_2 at the interface disappears because the value of E_{H_2} can be less than 1. The enrichment of both CO_2 and H_2 also decreases with the temperature in the mixture system, and H_2 enrichment disappears at 400 K in the system of CO_2/H_2 = 3:10.

The enrichment and surface excess are linked but do not contain the same information.[40,41] The surface adsorption of CO_2 and H_2 in different systems is shown in Figure 5. The CO_2 surface excess values are always positive, while the values of H_2 can be negative. The difference between the CO_2 and H_2 adsorption property is because CO_2 is quadrupole, which is capable of establishing a Debye interaction with H_2O, while there is only a weak vdW interaction between H_2 and H_2O. For pure CO_2, the surface excess increased to the peak value at 320 K and then decreased with the temperature. This agrees well with the work of Shiga et al.[37] that the surface excess of CO_2 at isobaric conditions always has the positive peak value appearing at the phase transition temperature when the pressure is less than 20 MPa. In a mixture system, the surface excess reduces gradually with the temperature, and the values for CO_2-dominated systems are much higher than those of H_2-dominated systems. The increase in the H_2 concentration can reduce the surface excess of CO_2. The surface excess of H_2 reduces with the temperature at pure H_2 and H_2-dominated mixture systems, with the values about 10^{-2} smaller than those of CO_2. In the CO_2-dominated system, the surface excess of H_2

https://doi.org/10.1021/acs.energyfuels.3c03164
Energy Fuels 2023, 37, 18986−18995

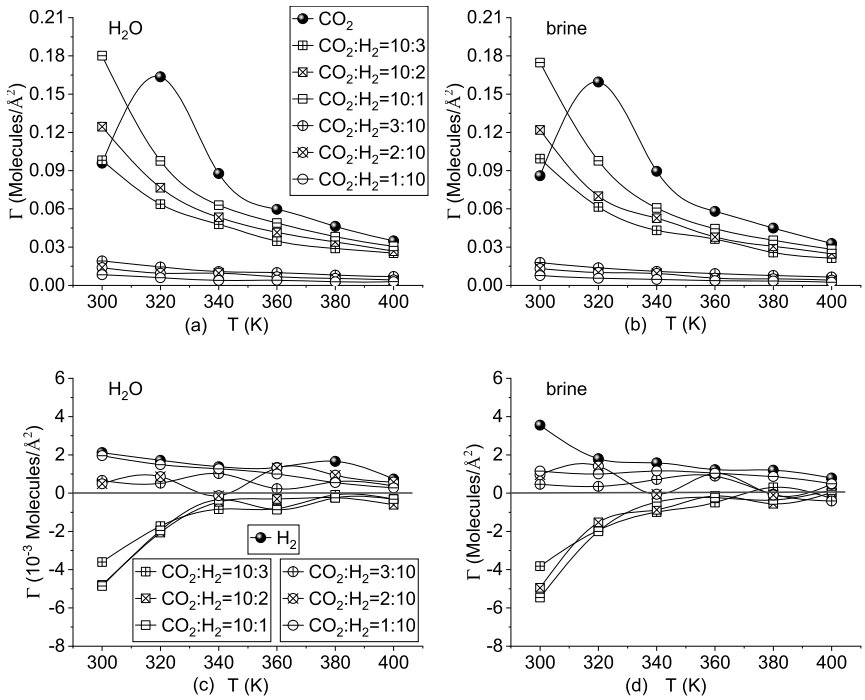

Figure 5. Effect of the temperature on the surface excess of gases: (a and b) surface excess of CO_2 and (c and d) surface excess of H_2.

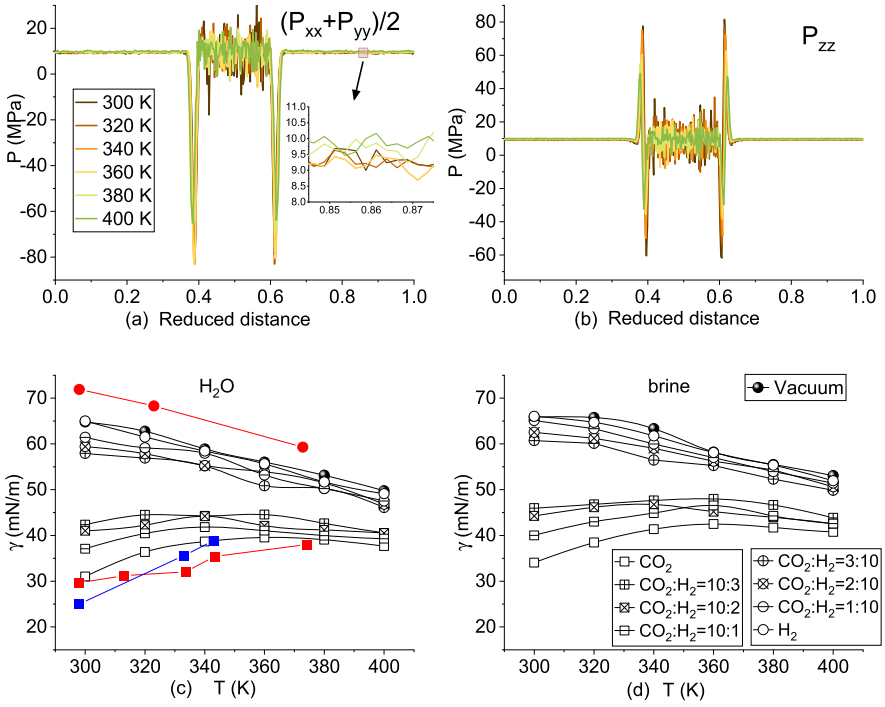

Figure 6. (a and b) Profile of the tangential and normal pressure components of the system CO_2/H_2 = 10:3 at H_2O. (c and d) Effect of the temperature on the IFT of different systems. The red solid circles are experimental data of the H_2-H_2O system adapted with permission from ref 47. Copyright 2018 Elsevier. The red solid squares are experimental data of the CO_2-H_2O system adapted with permission from ref 48. Copyright 2010 American Chemical Society. The blue solid squares are experimental data of the CO_2-H_2O system adapted with permission from ref 25. Copyright 2015 Elsevier.

is negative, increases gradually with the temperature, and reaches zero at about 340−360 K. The NaCl ions have limited effects on the surface excess.

Besides the density profile, the pressure profile and IFT of the gas−brine system are calculated and shown in Figure 6. The pressure profile in panels a and b of Figure 6 is calculated by the summation of the per atom stress tensor in each bin. The method developed by Irving−Kirkwood[42] is used to compute the IFT expressed in terms of the difference between the normal and tangential components of the pressure tensor[43]

https://doi.org/10.1021/acs.energyfuels.3c03164
Energy Fuels 2023, 37, 18986−18995

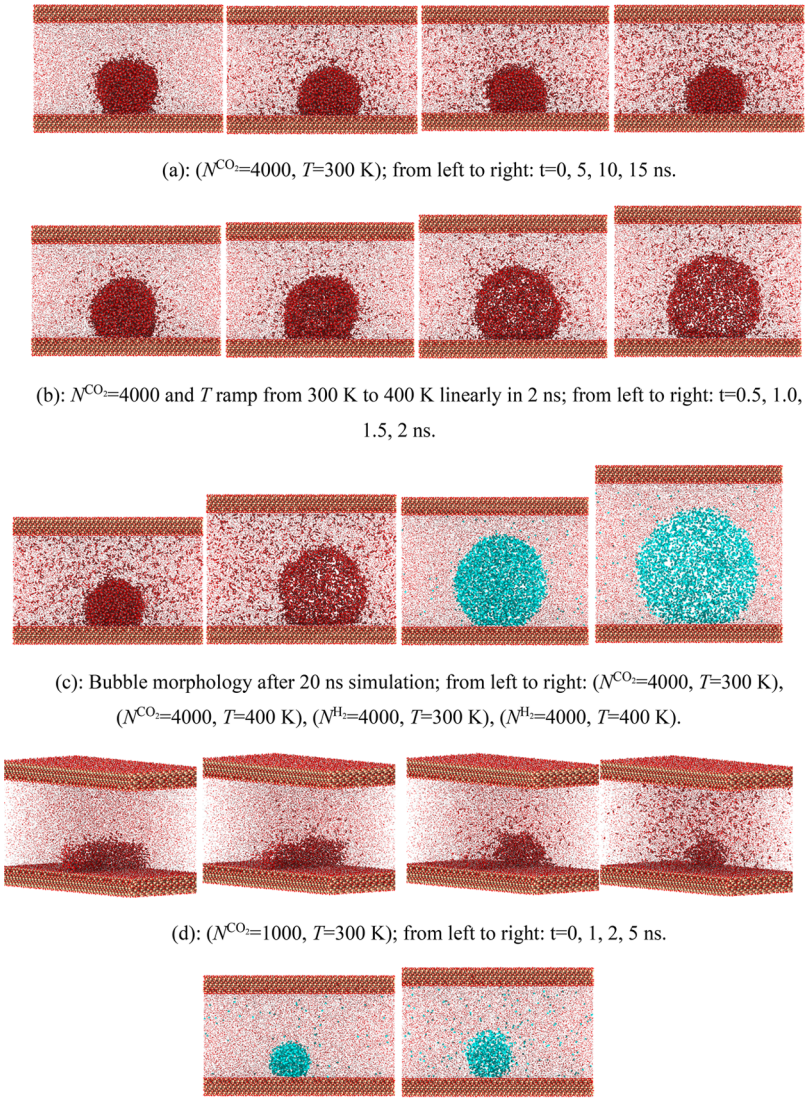

Figure 7. Effect of the system size and dissolution on bubble morphology at 300 and 400 K.

$$\gamma = \frac{1}{2}\int_{-L_z/2}^{L_z/2}\left[\langle P_{zz}(z)\rangle - \frac{\langle P_{xx}(z)\rangle + \langle P_{yy}(z)\rangle}{2}\right]\mathrm{d}z \tag{7}$$

or by

$$\gamma = \frac{L_z}{2}\left[\langle P_{zz}\rangle - \frac{\langle P_{xx}\rangle + \langle P_{yy}\rangle}{2}\right] \tag{8}$$

where $P_{\alpha\alpha}$ is the diagonal component of the pressure tensor and the pre-factor of $^1/_2$ considers the existence of two interfaces in the simulation box.

The average pressure of the gas phase is in the range of 9.5−10 MPa, which is a bit lower than the assigned value because the surface adsorption and dissolution reduce the molecular number in the gas phase. The tangential pressure tensor exhibits strong negative values, while the normal pressure tensor has a positive maximum value and a negative minimum value at the interfaces.[44,45] From panels c and d of Figure 6, IFTs of the brine system are higher than those of the H_2O system, which is consistent with the previous work of Zhao et al.,[46] who found that the incremental IFT ($\Delta\gamma = \gamma^{CO_2-brine} - \gamma^{CO_2-H_2O}$) increases linearly with the salinity. Pure H_2 can hardly alter the IFT, while CO_2 significantly reduces the IFT. It is because the electrostatic interactions between CO_2 and H_2O play an important role in virial anisotropy for the CO_2-H_2O system.[39] In H_2 and H_2-dominated systems, the IFT decreases linearly with the temperature for both H_2O and brine systems. Unlike the monotonous trend of the IFT with the CO_2 pressure at isothermal conditions,[39] the IFT increases with the temperature until it reaches the peak at about 320−360 K and then decreases with the temperature in pure CO_2 and CO_2-dominated systems.

3.2. Effect of the System Size and Gas Dissolution on Bubble Morphology. In MD simulation of the wettability using the sessile droplet method, it has been justified that the CA is independent of the size of the water droplet in cylindrical shape.[49] However, the effect of the system size (indicated by the number of gas molecules, N) and gas dissolution on bubble morphology is still lacking. The time evolution and temperature effect on bubble morphology of gases with N = 4000 and 2000 are shown in Figure 7. The system is maintained at 300 K for 20 ns or increased to 400 K in 2 ns followed by a 20 ns constant temperature simulation at 400 K. As expected, the size of the gas

https://doi.org/10.1021/acs.energyfuels.3c03164
Energy Fuels 2023, 37, 18986−18995

bubble would decrease with time as a result of the dissolution but increase with the temperature as a result of the expansion. The system size of $N = 4000$ is sufficient to maintain the bubble morphology for both CO_2 and H_2 in 300 and 400 K even after CO_2 dissolution completes and reaches saturation. However, the bubble would be disconnected at 300 K after 1 ns simulation in a smaller system of CO_2 with $N = 1000$, while this does not occur for H_2. The disconnected CO_2 bubble changes into a semi-spherical shape and continues the dissolution.

3.3. Effect of the Temperature on the Contact Angle. Considering that the significant difference of the dissolution of CO_2 and H_2 can alter the concentration of the mixtures inside the bubble after a long time evolution, the CAs of pure CO_2 and H_2 bubble are summarized in Table 1. The contact angle is computed by the two-dimensional (2D) density profiles of the gas and liquid. A circular profile is fitted at the gas−liquid interface, where the isodensity is in the range of 0.2−0.4 g/mL. The contact angle is determined by $\theta = \arccos\left(\frac{z_0 - b}{R}\right)$, where b is the coordinate of the center of the fitted circle in the z direction, R is the circle radius, and z_0 is the height of the contact plane.[49]

Table 1. CAs of CO_2 and H_2 at 300 and 400 K

CA (deg)		300 K	400 K
CO_2	H_2O	122.10	134.31
	brine	109.84	130.80
H_2	H_2O	155.80	156.84
	brine	146.68	151.04

The CAs of the CO_2 and H_2 bubbles are all greater than 100° in all conditions because the Q2 silica is strongly water-wet compared to gas-wet owing to the hydrogen bonding between water and the hydroxyl groups on the Q2 surface. The CAs of CO_2 are smaller than those of H_2 in the same conditions, which indicates that Q2 is more CO_2-wet than H_2-wet. NaCl ions can reduce the CAs because the ions can form the electrical double layer, which reduces the polarity of the silica surface, and this effect is more pronounced at a low temperature. CAs of CO_2 increase with the temperature for both H_2O and brine systems. This agrees with the work of Chen et al.,[50] using a sessile droplet surrounded by CO_2, where the CA of H_2O at 318 K and 9.5 MPa is 33°, which is reduced to 26.4° at 383 K and 26.4 MPa. For H_2, the effect of the temperature on CAs is not as pronounced as that of CO_2.

4. CONCLUSION

The MD simulation is performed to predict the interfacial properties of CO_2/H_2 mixtures contacting with the brine film at operation conditions of 10 MPa and the temperature ranging from 300 to 400 K. The morphology of gas bubbles in the gas−brine−rock system is investigated. The CAs of the CO_2 and H_2 bubbles are calculated. The conclusions are drawn as follows:

The dissolution of CO_2 in water and brine is much higher than that of H_2. NaCl ions reduce the diffusivity and solubility of CO_2 in the brine film. The temperature increases the diffusivity of CO_2 but reduces its solubility. CO_2 has a much stronger affinity than H_2 with H_2O at the interface, and the surface adsorption of H_2 is not as prominent as that of CO_2. The surface excess of H_2 can be negative in the CO_2-dominated mixture system. The interaction between H_2 and H_2O is too weak to alter the IFT under all conditions. The IFT reduces with the temperature monotonously at the H_2-dominated mixture system, while there would be peak values at about 320−360 K in the CO_2 and CO_2-dominated systems. NaCl ions can increase the IFT in all systems.

To use the bubble morphology for CA calculation, the initial size of the CO_2 bubble should be relatively larger to avoid the dissolution-induced disconnection. H_2 is much less wet than CO_2 on hydrophilic silica. NaCl ions reduce the CA of gas bubbles, especially at a low temperature. Unlike the CO_2 bubble, effect of the temperature on the CA of the H_2 bubble is not prominent.

■ ASSOCIATED CONTENT

Data Availability Statement

The data underpinning this publication can be accessed from the data repository of Brunel University London, Brunelfigshare, here under a CCBY license: https://figshare.com/articles/figure/Energy_and_Fuel/24282280.

■ AUTHOR INFORMATION

Corresponding Author

Jun Xia − *Department of Mechanical and Aerospace Engineering, Brunel University London, Uxbridge UB8 3PH, United Kingdom*; orcid.org/0000-0002-2547-3483; Email: jun.xia@brunel.ac.uk

Authors

Cheng Chen − *Department of Mechanical and Aerospace Engineering, Brunel University London, Uxbridge UB8 3PH, United Kingdom*

Hamid Bahai − *Department of Mechanical and Aerospace Engineering, Brunel University London, Uxbridge UB8 3PH, United Kingdom*

Complete contact information is available at: https://pubs.acs.org/10.1021/acs.energyfuels.3c03164

Notes

The authors declare no competing financial interest.

■ ACKNOWLEDGMENTS

This work was supported by the Engineering and Physical Sciences Research Council (EPSRC) under Grant EP/T033940/1. The authors are grateful to the high performance computing (HPC) resource of ARCHER2 supported by the EPSRC Access to High Performance Computing under Project e774 and UK Materials and Molecular Modelling Hub for computational resources, which is funded by EPSRC (EP/T022213/1, EP/W032260/1, and EP/P020194/1).

■ REFERENCES

(1) International Energy Agency (IEA). *CCUS in Clean Energy Transitions*; IEA: Paris, France, 2020; https://www.iea.org/reports/ccus-in-clean-energy-transitions.

(2) International Energy Agency (IEA). *The World Has Vast Capacity To Store CO_2: Net Zero Means We'll Need It*; IEA: Paris, France, 2021; https://www.iea.org/commentaries/the-world-has-vast-capacity-to-store-co2-net-zero-means-we-ll-need-it.

(3) Muhammed, N. S.; Haq, B.; Al Shehri, D.; Al-Ahmed, A.; Rahman, M. M.; Zaman, E. A review on underground hydrogen storage: Insight into geological sites, influencing factors and future outlook. *Energy Rep.* **2022**, *8*, 461−499.

(4) Bourg, I. C.; Beckingham, L. E.; DePaolo, D. J. The nanoscale basis of CO_2 trapping for geologic storage. *Environ. Sci. Technol.* **2015**, *49* (17), 10265−10284.

(5) Iglauer, S. CO_2−water−rock wettability: Variability, influencing factors, and implications for CO_2 geostorage. *Acc. Chem. Res.* **2017**, *50* (5), 1134−1142.
(6) Heinemann, N.; Alcalde, J.; Miocic, J. M.; Hangx, S. J. T.; Kallmeyer, J.; Ostertag-Henning, C.; Hassanpouryouzband, A.; Thaysen, E. M.; Strobel, G. J.; Schmidt-Hattenberger, C.; Edlmann, K.; Wilkinson, M.; Bentham, M.; Stuart Haszeldine, R.; Carbonell, R.; Rudloff, A. Enabling large-scale hydrogen storage in porous media—The scientific challenges. *Energy Environ. Sci.* **2021**, *14* (2), 853−864.
(7) Iglauer, S.; Mathew, M.; Bresme, F. Molecular dynamics computations of brine−CO_2 interfacial tensions and brine−CO_2−quartz contact angles and their effects on structural and residual trapping mechanisms in carbon geo-sequestration. *J. Colloid Interface Sci.* **2012**, *386* (1), 405−414.
(8) Iglauer, S.; Pentland, C.; Busch, A. CO_2 wettability of seal and reservoir rocks and the implications for carbon geo-sequestration. *Water Resour. Res.* **2015**, *51* (1), 729−774.
(9) Pan, B.; Yin, X.; Ju, Y.; Iglauer, S. Underground hydrogen storage: Influencing parameters and future outlook. *Adv. Colloid Interface Sci.* **2021**, *294*, No. 102473.
(10) Jun, Y.-S.; Zhang, L.; Min, Y.; Li, Q. Nanoscale chemical processes affecting storage capacities and seals during geologic CO_2 sequestration. *Acc. Chem. Res.* **2017**, *50* (7), 1521−1529.
(11) Chen, C.; Chai, Z.; Shen, W.; Li, W.; Song, Y. Wettability of supercritical CO_2−brine−mineral: The effects of ion type and salinity. *Energy Fuels* **2017**, *31* (7), 7317−7324.
(12) Wang, J.; Ryan, D.; Anthony, E. J.; Wildgust, N.; Aiken, T. Effects of impurities on CO_2 transport, injection and storage. *Energy Procedia* **2011**, *4*, 3071−3078.
(13) Mahmoodpour, S.; Amooie, M. A.; Rostami, B.; Bahrami, F. Effect of gas impurity on the convective dissolution of CO_2 in porous media. *Energy* **2020**, *199*, No. 117397.
(14) Li, D.; Zhang, H.; Li, Y.; Xu, W.; Jiang, X. Effects of N_2 and H_2S binary impurities on CO_2 geological storage in stratified formation—A sensitivity study. *Appl. Energy* **2018**, *229*, 482−492.
(15) Feldmann, F.; Hagemann, B.; Ganzer, L.; Panfilov, M. Numerical simulation of hydrodynamic and gas mixing processes in underground hydrogen storages. *Environ. Earth Sci.* **2016**, *75*, 1165.
(16) Tsuji, T.; Jiang, F.; Christensen, K. T. Characterization of immiscible fluid displacement processes with various capillary numbers and viscosity ratios in 3D natural sandstone. *Adv. Water Resour.* **2016**, *95*, 3−15.
(17) Yang, Y.; Narayanan Nair, A. K.; Sun, S. Molecular dynamics simulation study of carbon dioxide, methane, and their mixture in the presence of brine. *J. Phys. Chem. B* **2017**, *121* (41), 9688−9698.
(18) Yang, Y.; Narayanan Nair, A. K.; Anwari Che Ruslan, M. F.; Sun, S. Bulk and interfacial properties of the decane+water system in the presence of methane, carbon dioxide, and their mixture. *J. Phys. Chem. B* **2020**, *124* (43), 9556−9569.
(19) van Rooijen, W.; Habibi, P.; Xu, K.; Dey, P.; Vlugt, T.; Hajibeygi, H.; Moultos, O. Interfacial tensions, solubilities, and transport properties of the H_2/H_2O/NaCl system: A molecular simulation study. *J. Chem. Eng. Data* **2023**, DOI: 10.1021/acs.jced.2c00707.
(20) Pan, B.; Yin, X.; Iglauer, S. A review on clay wettability: From experimental investigations to molecular dynamics simulations. *Adv. Colloid Interface Sci.* **2020**, *285*, No. 102266.
(21) Chen, C.; Zhang, N.; Li, W.; Song, Y. Water contact angle dependence with hydroxyl functional groups on silica surfaces under CO_2 sequestration conditions. *Environ. Sci. Technol.* **2015**, *49* (24), 14680−14687.
(22) Aslannezhad, M.; Ali, M.; Kalantariasl, A.; Sayyafzadeh, M.; You, Z.; Iglauer, S.; Keshavarz, A. A review of hydrogen/rock/brine interaction: Implications for Hydrogen Geo-storage. *Prog. Energy Combust. Sci.* **2023**, *95*, No. 101066.
(23) Al-Yaseri, A.; Wolff-Boenisch, D.; Fauziah, C. A.; Iglauer, S. Hydrogen wettability of clays: Implications for underground hydrogen storage. *Int. J. Hydrogen Energy* **2021**, *46* (69), 34356−34361.
(24) Al-Yaseri, A.; Abdel-Azeim, S.; Al-Hamad, J. Wettability of water−H_2-quartz and water−H_2−calcite experiment and molecular dynamics simulations: Critical assessment. *Int. J. Hydrogen Energy* **2023**, DOI: 10.1016/j.ijhydene.2023.05.294.
(25) Sarmadivaleh, M.; Al-Yaseri, A. Z.; Iglauer, S. Influence of temperature and pressure on quartz−water−CO_2 contact angle and CO_2-water interfacial tension. *J. Colloid Interface Sci.* **2015**, *441*, 59−64.
(26) Potoff, J. J.; Siepmann, J. I. Vapor−liquid equilibria of mixtures containing alkanes, carbon dioxide, and nitrogen. *AIChE J.* **2001**, *47* (7), 1676−1682.
(27) Zhong, H.; Lai, S.; Wang, J.; Qiu, W.; Lüdemann, H.-D.; Chen, L. Molecular dynamics simulation of transport and structural properties of CO_2 using different molecular models. *J. Chem. Eng. Data* **2015**, *60* (8), 2188−2196.
(28) Zeron, I. M.; Abascal, J. L. F.; Vega, C. A force field of Li^+, Na^+, K^+, Mg^{2+}, Ca^{2+}, Cl^-, and SO_4^{2-} in aqueous solution based on the TIP4P/2005 water model and scaled charges for the ions. *J. Chem. Phys.* **2019**, *151* (13), No. 134504.
(29) Abascal, J. L. F.; Vega, C. A general purpose model for the condensed phases of water: TIP4P/2005. *J. Chem. Phys.* **2005**, *123* (23), No. 234505.
(30) Zeron, I. M.; Gonzalez, M. A.; Errani, E.; Vega, C.; Abascal, J. L. "In Silico" Seawater. *J. Chem. Theory Comput.* **2021**, *17* (3), 1715−1725.
(31) Wang, S.; Hou, K.; Heinz, H. Accurate and compatible force fields for molecular oxygen, nitrogen, and hydrogen to simulate gases, electrolytes, and heterogeneous interfaces. *J. Chem. Theory Comput.* **2021**, *17* (8), 5198−5213.
(32) Heinz, H.; Lin, T.-J.; Kishore Mishra, R.; Emami, F. Thermodynamically consistent force fields for the assembly of inorganic, organic, and biological nanostructures: the INTERFACE force field. *Langmuir* **2013**, *29* (6), 1754−1765.
(33) Emami, F. S.; Puddu, V.; Berry, R. J.; Varshney, V.; Patwardhan, S. V.; Perry, C. C.; Heinz, H. Force field and a surface model database for silica to simulate interfacial properties in atomic resolution. *Chem. Mater.* **2014**, *26* (8), 2647−2658.
(34) Plimpton, S. Fast parallel algorithms for short-range molecular dynamics. *J. Comput. Phys.* **1995**, *117* (1), 1−19.
(35) Stukowski, A. Visualization and analysis of atomistic simulation data with OVITO−the Open Visualization Tool. *Modell. Simul. Mater. Sci. Eng.* **2010**, *18* (1), No. 015012.
(36) Chen, C.; Xia, J.; Martinez, Q.; Jiang, X.; Bahai, H. Molecular dynamics of interfacial crystallization of dodecane on hydroxylated silica surface impacted by H_2O and CO_2. *J. Chem. Phys.* **2023**, *158* (20), No. 204708.
(37) Shiga, M.; Morishita, T.; Sorai, M. Interfacial tension of carbon dioxide−water under conditions of CO_2 geological storage and enhanced geothermal systems: A molecular dynamics study on the effect of temperature. *Fuel* **2023**, *337*, No. 127219.
(38) Li, X.; Ross, D. A.; Trusler, J. M.; Maitland, G. C.; Boek, E. S. Molecular dynamics simulations of CO_2 and brine interfacial tension at high temperatures and pressures. *J. Phys. Chem. B* **2013**, *117* (18), 5647−5652.
(39) Ji, J.; Zhao, L.; Tao, L.; Lin, S. Molecular Gibbs Surface Excess and CO_2-Hydrate Density Determine the Strong Temperature-and Pressure-Dependent Supercritical CO_2−Brine Interfacial Tension. *J. Phys. Chem. B* **2017**, *121* (25), 6200−6207.
(40) Stephan, S.; Langenbach, K.; Hasse, H. Interfacial properties of binary Lennard-Jones mixtures by molecular simulation and density gradient theory. *J. Chem. Phys.* **2019**, *150* (17), No. 174704.
(41) Stephan, S.; Cárdenas, H.; Mejía, A.; Müller, E. A. The monotonicity behavior of density profiles at vapor−liquid interfaces of mixtures. *Fluid Phase Equilib.* **2023**, *564*, No. 113596.
(42) Irving, J.; Kirkwood, J. G. The statistical mechanical theory of transport processes. IV. The equations of hydrodynamics. *J. Chem. Phys.* **1950**, *18* (6), 817−829.
(43) Mejia, A.; Cartes, M.; Segura, H.; Müller, E. A. Use of equations of state and coarse grained simulations to complement experiments: Describing the interfacial properties of carbon dioxide + decane and carbon dioxide + eicosane mixtures. *J. Chem. Eng. Data* **2014**, *59* (10), 2928−2941.

(44) Calvo, F. Molecular dynamics determination of the surface tension of silver−gold liquid alloys and the Tolman length of nanoalloys. *J. Chem. Phys.* **2012**, *136* (15), No. 154701.
(45) Martínez-Ruiz, F. J.; Blas, F. J.; Mendiboure, B.; Moreno-Ventas Bravo, A. I. Effect of dispersive long-range corrections to the pressure tensor: The vapour−liquid interfacial properties of the Lennard-Jones system revisited. *J. Chem. Phys.* **2014**, *141* (18), No. 184701.
(46) Zhao, L.; Ji, J.; Tao, L.; Lin, S. Ionic effects on supercritical CO_2−brine interfacial tensions: Molecular dynamics simulations and a universal correlation with ionic strength, temperature, and pressure. *Langmuir* **2016**, *32* (36), 9188−9196.
(47) Chow, Y. F.; Maitland, G. C.; Trusler, J. M. Interfacial tensions of (H_2O + H_2) and (H_2O + CO_2 + H_2) systems at temperatures of (298−448) K and pressures up to 45 MPa. *Fluid Phase Equilib.* **2018**, *475*, 37−44.
(48) Georgiadis, A.; Maitland, G.; Trusler, J. M.; Bismarck, A. Interfacial tension measurements of the (H_2O + CO_2) system at elevated pressures and temperatures. *J. Chem. Eng. Data* **2010**, *55* (10), 4168−4175.
(49) Silvestri, A.; Ataman, E.; Budi, A.; Stipp, S.; Gale, J. D.; Raiteri, P. Wetting properties of the CO_2−water−calcite system via molecular simulations: shape and size effects. *Langmuir* **2019**, *35* (50), 16669−16678.
(50) Chen, C.; Dong, B.; Zhang, N.; Li, W.; Song, Y. Pressure and temperature dependence of contact angles for CO_2/water/silica systems predicted by molecular dynamics simulations. *Energy Fuels* **2016**, *30* (6), 5027−5034.

https://doi.org/10.1021/acs.energyfuels.3c03164
Energy Fuels 2023, 37, 18986−18995